Broadband trailing-edge noise prediction with a stochastic source model

I.F. Cozza, A. Iob, R. Arina *

DIASP – Politecnico di Torino, Corso Duca degli Abruzzi 24, 10129 Torino, Italy

A B S T R A C T

A RANS-based numerical technique for the prediction of the airfoil trailing-edge broadband noise is presented. The definition of the sound sources from RANS turbulence statistics is based on a stochastic reconstruction of the turbulent velocity fluctuations. The method, named Eulerian Solenoidal Digital Filter, accounts for the convective transport and for the solenoidality of the velocity field. The acoustic near field is computed solving the Acoustic Perturbation Equations in the frequency domain. The integral formulation of Ffowcs Williams and Hawkings is used to evaluate the far-field radiation. The ESDF method is validated for the case of homogeneous isotropic turbulence and it is applied to the calculation of the broadband trailing-edge noise of a NACA 0012 airfoil. Near-field and far-field results are compared with analytical and experimental data.

1. Introduction

Broadband trailing-edge boundary-layer (TE-BL) noise is one of the most challenging issues for the aeroacoustic research, as it occurs in many technical situations, like airframe noise, or turbomachinery noise. TE-BL noise is due to the scattering of the acoustic disturbances induced by the boundary-layer turbulent structures over the trailing-edge geometry, changing the source from a quadrupolar structure to a more efficient dipolar character [1].

Broadband TE-BL noise prediction techniques based on Large Eddy Simulation (LES) for the evaluation of the noise sources, and on the acoustic analogy for the computation of the acoustic radiation, are accurate and reliable. However their high computational cost prevents them to be applied as an aeroacoustic design and optimization tool. LES computations of realistic configurations with accurate space–time correlations are out of the range for industrial applications, when several configurations have to be studied. In order to introduce the broadband noise prediction in the industrial design, a less computationally intensive procedure should be developed. An interesting alternative approach has been recently proposed by Casalino et al. [2] for low-speed fan noise predictions. It consists in applying a Ffowcs Williams and Hawkings acoustic analogy to the wall pressure field computed with the unsteady incompressible Reynolds Averaged Navier–Stokes (RANS) equations, with superimposed a stochastic reconstruction of broadband fluctuations. It is an interesting methodology for rotating configurations. In the case of an isolated airfoil with low-speed flow, statistically stationary in time, a further simplification is possible [3]: compute the mean flow field with the steady incompressible RANS and use a stochastic method to synthesize a random turbulent field, representing the key features of the sound sources of acoustic propagation model.

Steady-state RANS simulations are a standard tool for aerodynamic design, as they are computationally efficient, but they only provide the turbulence statistics. Nevertheless the far-field spectrum of an acoustic variable depends only on the two-point space–time correlations of the sound sources. On this basis, many techniques for the definition of the sound sources from RANS calculations have been developed based on stochastic reconstruction of the turbulence fluctuations. Kraichnan [4] proposed the first stochastic method based on a decomposition in random Fourier modes. Further developing this approach, Béchara et al. [5] proposed the Stochastic Noise Generation and Radiation (SNGR) technique and applied it to the case of noise generation in free turbulent flows. Bailly et al. [6] extended the method to predict the noise radiation from subsonic and supersonic jets. Billson et al. [7] introduced the idea of applying a digital time-filter and a convection operator in the SNGR technique, in order to prevent the shear layer decorrelation and to account for the convection of the noise sources. In recent years, other authors [8,9] applied the SNGR technique to trailing-edge noise predictions. Another impor-tant class of stochastic procedures is based on the reconstruct of the turbulence fluctuations applying a digital space-filter to a ran-dom field. These methods have been first introduced by Careta et al. [10] and Klein et al. [11]. Ewert extended this approach in the Random Particle Mesh (RPM) method [12], introducing a Lagrangian particle approach for the convection of the turbulent fluctuations, a stream function formulation for the space-filtered quantities in order to enforce the solenoidality of the turbulent

* Corresponding author.
E-mail address: renzo.arina@polito.it (R. Arina).

velocity field, and the solution of a Langevin equation for the time-decorrelation. The RPM method has been successfully applied to slat noise [12], trailing-edge noise [13], combustion noise [14] and cabin noise [15] problems. A similar technique has been devel-oped by Dieste and Gabard [16] for fan interaction noise.

In this paper we describe a fast and reliable method, termed Eulerian Solenoidal Digital Filter (ESDF), for the reconstruction of the turbulent noise sources from the turbulence statistics (turbulent kinetic energy and dissipation), obtained with RANS calculations for low Mach number flows. Like the RPM method, the ESDF belongs to the class of the digital filter-based stochastic turbulence methods. The main objective of the present work is to modify the classical RPM method [12] introducing a stream-function formulation and adopting an Eulerian approach to solve a scalar transport equation for the reconstructed stream-function. The ESDF method guarantees that velocity fluctuations satisfy the solenoidal property. This additional constraint is very important for a correct noise source identification. The Eulerian approach enables an easy extension of the present method to complex three-dimensional configurations. The time correlation is enforced applying the Billson's time digital filter [7]. The acoustic propagation model is composed by a near-field propagation model, based on the Acoustic Perturbation Equations [12], to account for the non-uniformities in the mean flow, and a far-field propagation model based on the Ffwocs Williams and Hawking acoustic analogy. To assess the uncertainties connected with the basic assumptions in the stochastic model, a detailed analysis of the choices of the constant values is made.

In Section 2 the ESDF method is presented. Its numerical implementation and the acoustic propagation model are described in Section 3. The technique is validated for the case of two-dimensional homogeneous and isotropic turbulence, and is used to study the noise emission of low Mach number flows over a NACA 0012 (Section 4) in order to demonstrate the capability of the ESDF method to evaluate the sound sources and of the coupled propagation model to represent the near-field and far-field noise radiation for the broadband trailing edge noise problem.

2. Eulerian Solenoidal Digital Filter method

2.1. Stochastic source modeling

Broadband noise sources are function of fluctuating turbulent velocities, therefore the knowledge of the latter is required for their identification. On the other hand, RANS calculations do not explicitly provide the turbulent fluctuations but only space–time statistical values, like turbulent kinetic energy k and turbulent dissipation frequency ω_{Rans}. Unsteady-RANS models do not fill this gap, as they only provide some more information concerning large scale tonal noise. Therefore a stochastic reconstruction strategy must be introduced to estimate the fluctuations starting from the statistical values obtained with RANS calculations.

Being $\Gamma(\boldsymbol{x},t)$ a turbulent fluctuating quantity, and $R(\boldsymbol{x},\boldsymbol{r},\tau)=\overline{\Gamma(\boldsymbol{x},t)\Gamma(\boldsymbol{x}+\boldsymbol{r},\,t+\tau)}$ its two-point space–time correlation function, a combination of a Gaussian correlation in space with an exponential correlation in time represents a simple correlation model:

$$R(\boldsymbol{x},\boldsymbol{r},\tau)=\widetilde{R}\exp\left[-\frac{\tau}{\tau_s}-\frac{\pi(\boldsymbol{r}-\boldsymbol{u_c}\tau)^2}{4l_s^2}\right], \tag{1}$$

where l_s and τ_s are the turbulent integral length and time scale respectively, and $\widetilde{R}$ is related to the r.m.s. value of the turbulent quantity for vanishing time and space separation. The convection speed $\boldsymbol{u_c}$ accounts for the Taylor hypothesis for the turbulent structures. In general, for non-homogeneous turbulence, l_s, τ_s and $\widetilde{R}$ are functions of position $\boldsymbol{x}$.

The aim of the stochastic reconstruction is to generate a fluctuating quantity $\Gamma(\boldsymbol{x},t)$ capable of reproducing the correlation described in Eq. (1). One possibility is to apply a digital filter to a white noise field, as originally proposed by Klein et al. [11]. Given a white noise field $\mathcal{U}(\boldsymbol{x})$, with statistical properties:

$$\begin{cases}\overline{\mathcal{U}(\boldsymbol{x})}=0,\\ \overline{\mathcal{U}(\boldsymbol{x})\mathcal{U}(\boldsymbol{x}+\boldsymbol{r})}=\delta(\boldsymbol{r}),\end{cases} \tag{2}$$

where δ is the Dirac delta function, a multidimensional space digital filter function can be defined as:

$$\Psi(\boldsymbol{x})=\int_{S_A}\widetilde{A}(\boldsymbol{x}')K^0(|\boldsymbol{x}-\boldsymbol{x}'|,l_s(\boldsymbol{x}'))\mathcal{U}(\boldsymbol{x}')d\boldsymbol{x}', \tag{3}$$

where S_A is a restricted source region, K^0 an appropriate filter kernel and $\widetilde{A}(\boldsymbol{x}')$ a local filter amplitude. It is important to remark that all the parameters in Eq. (3) are varying in space. The filter kernel is normalized in order to have $\overline{\Psi(\boldsymbol{x},t)\Psi(\boldsymbol{x}+\boldsymbol{r},t+\tau)}=1$ when $\widetilde{A}=1$. Klein et al. [11] adopted this procedure to obtain space-filtered velocity fields, applying Eq. (3) to each individual velocity component with different sets of white noise fields. A similar technique was devised by Mesbah [17] to generate source terms for aeroacoustic calculations. If the velocity field is directly evaluated by applying Eq. (3), no hypothesis is made on the solenoidal property of the reconstructed velocity. At low and moderate Mach numbers, the turbulent field can be considered as incompressible, therefore the fluctuating velocities are divergence free. If this constrain is not respected, important spurious noise sources may be introduced in the aeroacoustic solution. To enforce the solenoidal property of the generated field, a stream function of the velocity field can be reconstructed instead of the velocity itself. For a two-dimensional field, given the stream function defined in Eq. (3), the corresponding velocity field is

$$\begin{cases}(\boldsymbol{u}_{turb})_x(\boldsymbol{x})=\frac{\partial\Psi(\boldsymbol{x})}{\partial y},\\ (\boldsymbol{u}_{turb})_y(\boldsymbol{x})=-\frac{\partial\Psi(\boldsymbol{x})}{\partial x}.\end{cases} \tag{4}$$

Following Careta et al. [10], it can be shown that all the properties of an isotropic and homogeneous turbulent velocity field in two dimensions (i.e. with constant parameters in Eq. (3)) can be reproduced by a fluctuating stream-function having an appropriate correlation. For the case of homogeneous and isotropic turbulence, the velocity correlation function

$$R_{ij}(\boldsymbol{r},\tau)=\overline{[\boldsymbol{u}_{turb})(\boldsymbol{x},t)]_i[\boldsymbol{u}_{turb}(\boldsymbol{x}+\boldsymbol{r},t+\tau)]_j}, \tag{5}$$

can be written in terms of longitudinal $f(\boldsymbol{r})$ and lateral $g(\boldsymbol{r})$ correlation functions. In the case of time separation $\tau=0$, it reads:

$$R_{ij}(\boldsymbol{r},0)=[f(\boldsymbol{r})-g(\boldsymbol{r})]n_in_j+g(\boldsymbol{r})\delta_{ij}, \tag{6}$$

where n_i is the unit versor. Since the field is solenoidal, the correlation functions $f(\boldsymbol{r})$ and $g(\boldsymbol{r})$ must satisfy an additional constrain which in two dimensions writes:

$$g(\boldsymbol{r})=f(\boldsymbol{r})+\boldsymbol{r}\frac{\partial f(\boldsymbol{r})}{\partial\boldsymbol{r}}. \tag{7}$$

It follows that if we define the scalar correlation function $C(\boldsymbol{r})=\Psi(\boldsymbol{x})\Psi(\boldsymbol{x}+\boldsymbol{r})$, $f(\boldsymbol{r})$ and $g(\boldsymbol{r})$ can be expressed as follows, because of Eq. (7),

$$\begin{cases}f(\boldsymbol{r})=-\frac{1}{\boldsymbol{r}}\frac{\partial C(\boldsymbol{r})}{\partial\boldsymbol{r}},\\ g(\boldsymbol{r})=-\frac{1}{\boldsymbol{r}}\frac{\partial^2 C(\boldsymbol{r})}{\partial\boldsymbol{r}^2}.\end{cases} \tag{8}$$

Normalizing the correlation R_{ij} in Eq. (1) with $2l_s^2/\pi$, for $\tau=0$, from Eqs. (6) and (8) it is possible to express the longitudinal correlation function $f(\boldsymbol{r})$ as

$$f(\boldsymbol{r}) = e^{-\frac{\pi r^2}{4 l_s^2}}, \tag{9}$$

and the corresponding integral length scale is

$$l = \int_0^\infty f(\boldsymbol{r}) d\boldsymbol{r} = \int_0^\infty e^{-\frac{\pi r^2}{4 l_s^2}} d\boldsymbol{r} = l_s, \tag{10}$$

which is coincident with the mean turbulent integral length scale as expected.

To obtain a fluctuating stream function with normalized longitudinal correlation function expressed by relation (9), it is possible to note that the normalized function

$$C^0(\boldsymbol{r}) = \frac{\overline{\Psi(\boldsymbol{x})\Psi(\boldsymbol{x}+\boldsymbol{r})}}{\overline{\Psi(\boldsymbol{x})\Psi(\boldsymbol{x})}}, \tag{11}$$

satisfying the condition $C^0(0) = 1$, can be related to the filter kernel throughout Eq. (3),

$$C^0(\boldsymbol{r}) = \int\int_{S_A} K^0(\xi) K^0(\boldsymbol{r} - \xi) d\xi = K^0 * K^0, \tag{12}$$

with unitary amplitude $\widetilde{A}$. Hence, it is possible to show that a Gaussian correlation function

$$C^0(\boldsymbol{r}) = e^{-\frac{\pi r^2}{4 l_s^2}} \tag{13}$$

is obtained applying a Gaussian shaped filter kernel

$$K^0(\boldsymbol{r}) = e^{-\frac{\pi r^2}{2 l_s^2}}. \tag{14}$$

A similar analysis can be carried out for three-dimensional turbulent fields, if the scalar stream-function is replaced by a solenoidal vector-potential by means of the Helmholtz theorem.

2.2. Eulerian Solenoidal Digital Filter

Using the filter relation (3), with the Gaussian filter kernel expressed in Eq. (14), it is possible to obtain a space-correlated solenoidal turbulent fluctuating velocity field. The separability property of the Gaussian kernel can be used to reduce the computational cost of the filter operation. The filter kernel in Eq. (3) is obtained as product of three one-dimensional kernels

$$K^0(\boldsymbol{x}) = K^0(x) K^0(y) K^0(z). \tag{15}$$

Evaluating the filter as a sequence of one-dimensional filters gives a speedup of a factor 10 with respect to a straightforward implementation in two-dimensional calculationsA. After the application of the space filter, the stream function $\Psi(\boldsymbol{x})$ is correlated in space, but it is uncorrelated in time, like white noise. To obtain an exponential time correlation as required by the model correla-tion (Eq. (1)), following Billson [7,18] a digital time filter must be applied to $\Psi(\boldsymbol{x})$:

$$\Psi_f^m(\boldsymbol{x}) = a \Psi_f^{m-1}(\boldsymbol{x}) + b \Psi^m(\boldsymbol{x}), \tag{16}$$

with

$$\begin{cases} a = e^{-\frac{\Delta t}{\tau}}, \\ b = \sqrt{1 - a^2}, \end{cases} \tag{17}$$

where Δt is the time-step, the m index represents the m-th realization of the turbulent field and $(\cdot)_f$ stands for time-filtered. The expression for b is a consequence of the constraint of keeping the r.m.s. of Ψ_f^m equal to the r.m.s of Ψ^m. The convection property is introduced in the noise source model solving a scalar transport equation for the $\Psi_f^{m-1}(\boldsymbol{x})$ field of the time filter (Eq. (16)):

$$\frac{\partial \Psi_f^{m-1}(\boldsymbol{x})}{\partial t} + \boldsymbol{U}_0(\boldsymbol{x}) \cdot \nabla \Psi_f^{m-1}(\boldsymbol{x}) = 0, \tag{18}$$

where $\boldsymbol{U}_0(\boldsymbol{x})$ is the mean flow velocity, obtained from the RANS solution. In the original formulation of Billson, the convection operator is applied to the fluctuating velocities. In this way the divergence-free property is not guaranteed in presence of non-uniform mean flow. Applying the convection operator to the reconstructed stream function, the lack of solenoidality is overcome. The reconstructed turbulent velocity fluctuations are evaluated from Eq. (4). The free parameters in the ESDF model are evaluated from the mean statistical results of the RANS simulation. The filter kernel amplitude $\widetilde{A}(\boldsymbol{x})$ can be evaluated inserting relation (3), in conjunction with the stream function definition (4), in the definition of the turbulent kinetic energy for a two-dimensional flow field, and enforcing the statistical properties (2):

$$k = \frac{1}{2}\left(\overline{(\boldsymbol{u}_{turb})_x^2(\boldsymbol{x})} + \overline{(\boldsymbol{u}_{turb})_y^2(\boldsymbol{x})}\right) = \frac{1}{2}\int\int_{S_A} \widetilde{A}^2 \left(\frac{\partial K^{0^2}}{\partial x} + \frac{\partial K^{0^2}}{\partial y}\right) d\boldsymbol{x}'. \tag{19}$$

Considering $\widetilde{A}(\boldsymbol{x})$ to be slowly varying on a distance $O(l_s)$, it is possible to take it out of the integral in Eq. (19), and using expression (14) for the filter kernel, it follows:

$$\widetilde{A}(\boldsymbol{x}) = \sqrt{\frac{2}{\pi} k(\boldsymbol{x})}. \tag{20}$$

The turbulent length and time scales can be derived from the statistical field provided by the RANS calculation, as follows:

$$\begin{cases} l_s = \max\left(l_{s,min}, \frac{C_l}{C_\mu}\frac{\sqrt{k}}{\omega_{Rans}}\right), \\ \tau_s = \frac{1}{C_\mu \omega_{Rans}}, \end{cases} \tag{21}$$

where ϵ is the turbulent dissipation. As suggested by Bailly and Juvé [19], the values of the parameters C_μ and C_l adopted for the computations of the noise sources are $C_\mu = 0.09$ and $C_l = 0.54$. Setting the value of the length-scale is equivalent to definying the smallest scales in the source region and therefore it is strictly related to the definition of the computational grid on which the stochastic reconstruction is made. The limiter in Eq. (21) has been introduced by Ewert [13] in order to prevent the appearance of unresolved length scales on the coarser acoustic mesh. When the turbulent length scale is limited, the filter amplitude in Eq. (20) must be slightly reduced in order to remove the amount of energy in the turbulent spectrum related to the filtered high frequencies.

3. Computational method

3.1. Mean flow field computation

The mean flow simulations are performed with OpenFOAM®[20], an open source collection of C++ libraries, solving the stea-dy-state incompressible RANS, with the Menter k–ω SST turbu-lence model [21]. The equations are discretized adopting a collocated Finite Volume method. Depending on the test case, the SIMPLE and PISO algorithms have been used in order to avoid pressure-related oscillations. A 2nd order Gamma scheme [22] has been employed, in conjunction with an Algebraic Multi-Grid linear system solver. In conjunction with the PISO algorithm, a 2nd order implicit backward scheme has been used for time integration. Both multi-block structured and unstructured meshes have been employed for the calculations. All the meshes were generated with the open source software *Gmsh* [23].

Several computations have been performed on different grids, with increased mesh resolution, in order to guarantee a converged solution in space. Because the main objective of the paper is the study of the noise source reconstruction model, the reported mean flow field computations are relative to the finer converged grid only.

3.2. Numerical implementation of the ESDF method

The coupling of the stochastic model, described in Section 2.2, with the aeroacoustic simulation, is a 3-step procedure:

1. The RANS solution is mapped onto a mesh localized in the active source region.
2. Noise sources are evaluated using the velocity fluctuations reconstructed with the ESDF model.
3. The noise sources are mapped onto the acoustic mesh.

The mapping onto the acoustic mesh is a key step in the procedure. Under-resolution of the source region in the acoustic simulation can generate spurious noise. Moreover, another source of spurious noise can be deemed to the abrupt truncation of the active source region along the mean flow direction [24,25]. To overcome these problems, the acoustic mesh has been refined in the active source region, and a Hann windowing of the data has been applied in the direction parallel to the mean flow at the inlet and outlet of each source patch.

No Lagrangian intermediate mesh has been used in the procedure, with benefits on the computational accuracy and efficiency, because no extra-mapping is needed. The source generation procedure is a stand-alone preprocessing for the acoustic calculation. The ESDF model has been implemented in C++, in the OpenFOAM® framework.

3.3. Three-dimensional far-field noise intensity estimation from two-dimensional data

To compare the two-dimensional simulations with experimental acoustic results, a scaling technique has been adopted to take into account the differences in the far-field decay of the acoustic pressure between two-dimensional and three-dimensional waves. This method is based on two assumptions: the geometry has to be equal in the spanwise direction, and the turbulent sources in the spanwise direction are statistically homogeneous. This procedure was originally adopted to reduce the computational effort of Large Eddy simulations for aeroacoustics, as it gives the possibility to obtain the correct far-field spectrum of long-span cylindrical bodies resolving only a small spanwise extension [26]. Following Ewert et al. [13], the correction applies only to the far-field acoustic pressure power spectral density G_{pp}, and reads:

$$G_{pp}|_{3D} = \frac{\omega l_z(\omega) S}{2\pi c_\infty R} G_{pp}|_{2D}, \tag{22}$$

where l_z is the spanwise coherence length scale, ω the angular frequency, S the span of the body, R the distance from the trailing-edge, and c_∞ the far-field speed of sound. The term l_z can be esti-mated from measurements, or modeled using semi-empirical tech-niques. A well known model for the spanwise coherence length, proposed by Corcos [27], i s

$$l_z = \frac{\beta U_c}{\omega}, \tag{23}$$

where β is an empirical constant, and U_c is the convection speed of the turbulent structures in the boundary layer, usually evaluated as a fraction of the external velocity U_e:

$$U_c = (0.7 \div 0.9) U_e. \tag{24}$$

Such a modelization of the convection speed is widely accepted in boundary layer turbulence studies when the Taylor hypothesis of frozen turbulence is valid. It may be questionable if a unique value in the range $(0.7 \div 0.9)U_e$ could be selected for the all airfoil cases. Nonetheless, Rozemberg [28] showed that a 30% variation of the convection velocity U_c may produce a 1.4dB shift in the far-field spectra evaluated with the extended-Amiet analytical model proposed by Roger and Moreau [29].

The constant β, as it is related to the geometry of the body, in principle should be specified for each case. However, the large number of measurements of this constant provided by the literature gives an appropriate database to apply the Corcos law to different cases. Moreover, Gruber and Joseph [30] observed a weak dependence of the value of β from the mean-flow velocity and incidence. Typical values of β, measured for various types of airfoils at different incidences and velocities, are in the range $1.4 \div 1.8$.

3.4. Noise radiation

The acoustic propagation in a medium with non-uniform mean flow, neglecting entropy fluctuations and fluid viscosity, is governed by the Acoustic Perturbation Equations (APE) [12], which read, in Cartesian coordinates and quasi-linear form,

$$\frac{\partial \mathbf{q}}{\partial t} + \boldsymbol{A}' \frac{\partial \mathbf{q}}{\partial x} + \boldsymbol{B}' \frac{\partial \mathbf{q}}{\partial y} + \boldsymbol{C}' \mathbf{q} = \mathbf{S}, \tag{25}$$

where $\mathbf{q} = \mathbf{q}(\boldsymbol{x},t) = [\rho', u', v', w', p']^T$ is the acoustic perturbation vector and $\mathbf{S} = \mathbf{S}(\boldsymbol{x},t)$ is the turbulent source term. $\boldsymbol{A}'$,$\boldsymbol{B}'$ and $\boldsymbol{C}'$ are the Jacobian matrices of the fluxes.

Considering a harmonic mode, with angular frequency ω:

$$\begin{cases} \mathbf{q} = Re(\hat{\mathbf{q}}(\mathbf{x},\omega) e^{i\omega t}), \\ \mathbf{S} = Re(\hat{\mathbf{S}}(\mathbf{x},\omega) e^{i\omega t}), \end{cases} \tag{26}$$

it is possible to transform the APE (Eq. (25)) into the frequency domain:

$$\boldsymbol{A} \frac{\partial \hat{\mathbf{q}}}{\partial x} + \boldsymbol{B} \frac{\partial \hat{\mathbf{q}}}{\partial y} + \boldsymbol{C} \hat{\mathbf{q}} = \hat{\mathbf{S}}. \tag{27}$$

The continuity equation in the APE is decoupled, hence it is possible to solve only the momentum and energy equations, and evaluate the density fluctuations, assuming homoentropic propagation, from the isentropic relation $\rho' = p'/{c_0}^2$. Density fluctuations are computed only in the far-field, where the homoentropic assumption holds, as input data for the Ffowcs Williams and Hawkings integral formulation. The source term $\mathbf{S}$ is a function of the turbulent velocity fluctuations. In the case of vortical fluctuations, applying the Lamb vector formulation [13], the linearized source term can be expressed in the form

$$\mathbf{S}(\mathbf{x},t) = \begin{pmatrix} 0 \\ \Omega_0 (u_{turb})_y + \Omega_{turb} v_0 \\ -\Omega_0 (u_{turb})_x - \Omega_{turb} u_0 \\ 0 \end{pmatrix}, \tag{28}$$

where Ω_0 and Ω_{turb} are the mean and turbulent vorticity fields respectively,

$$\begin{cases} \Omega_0 = \nabla \times \mathbf{U}_0, \\ \Omega_{turb} = \nabla \times (\mathbf{u}_{turb})_f. \end{cases} \tag{29}$$

The Fourier transform of the source term is evaluated numerically with a Fast Fourier Transform algorithm with appropriate filters (Tukey windowing, Band-Pass filter). The APE (27) are discretized using a Galerkin Finite Element method [31] and Perfectly Matched Layer (PML) [32] non-reflecting boundary conditions are imposed along the far-field boundaries.

The Ffowcs Williams and Hawkings integral formulation [33] is applied to evaluate the far-field propagation. The near-field acoustic variables, solution of the APE, are extracted on a permeable integration path located in the uniform flow region and are propagated to the far field.

4. Results

4.1. ESDF validation

The capability of the ESDF method to reconstruct a turbulent velocity field with given first and second order statistics, is verified in the case of two-dimensional homogeneous and isotropic turbulence in a square, with known exact analytical space and time corre-lation functions. The two-dimensional turbulence is generated in a square with side 0.006 m long on a uniform Cartesian mesh of 1×10^{-4} m grid size. The reference conditions in the square are $\mathbf{U}_0(\mathbf{x}) = 0$ m/s, $k = 1$ m^2/s^2 and $\omega_{Rans} = 1000$ 1/s. To compare with the analytical results, the length and time scales have been chosen a priori. Setting a turbulent length-scale $l_s = 1 \times 10^{-2}$ m and a time-scale $\tau_s = 1.111 \times 10^{-2}$ s, both the parameters C_l and C_μ in Eq.(21) have been set, for this specific test case, equal to 0.09. The asso-ciated constant filter amplitude is $\tilde{A}(\mathbf{x}) = 0.798$ m/s. For each source cell, the truncation value K^0_{min} in Eq. (3) is 1×10^{-3}. This value has been found to be a good compromise between accuracy of the recon-struction and computational efficiency. In Fig. 1a the vector plot of the reconstructed velocity fluctuations $\boldsymbol{u}_{turb}$, is shown. The time his-tory of the reconstructed turbulent kinetic energy in the probe point $\boldsymbol{x} = (0, 0)$ m is shown in Fig. 1b. After a transient, the target value given by the mean field k is recovered, confirming that the ESFD method reproduces the target energy content in the turbulent veloc-ity field. The normalized space correlations R_{uu} and R_{vv} for an hori-zontal probe line are compared in Fig. 2a with the analytical correlations given in Eq. (6). A good agreement is obtained for both correlations. The time autocorrelation, corresponding to the time filter (Eq. (16)), is a decaying exponential as specified by the model correlation (1). The numerical and analytical normalized autocorre-lations are compared in Fig. 2b.

In order to verify the convection property of the generated field, a second test has been carried out on the same computational domain, with the same turbulent length and time-scales, and with a convection velocity $\mathbf{U}_0(\mathbf{x}) = 2$ m/s. Periodic boundary conditions have been adopted in the convection operator for the inlet and outlet boundaries. A convective time-scale is defined as follows:

$$\tau_c = \frac{l_s}{U_c}, \tag{30}$$

representing the time needed by an eddy convected by the mean flow to cover one turbulent length scale. In this case $\tau_c = 5 \times 10^{-3}$ s, and the ratio between the latter and the turbulent time scale is 0.5. In Fig. 3, the normalized cross-correlation of the fluctuating stream-function has been compared with the analytical relation (1). Seven probes with an even spacing of $l_s/2$ are selected to evaluate the cross-correlation, using the central probe as reference point. Numerical and analytical results are in good agreement. The cross correlation evaluated in probe locations that are upstream to the central one exhibit a monotonic decay, whereas a peak that is shifting to higher separation times is evident in the cross-correlations in the downstream probes. This behavior confirms that the ESDF procedure is able to correctly model the convection of turbulent structures.

4.2. NACA 0012 airfoil noise prediction

The noise generation by the turbulent flow field around a NACA 0012 airfoil at zero incidence and its radiation are investigated. The airfoil has a sharp trailing edge, in order to avoid tonal noise generation due to the vortex shedding. The airfoil chord is $c = 0.3048$ m, and the span is $S = 0.4572$ m. Four different mean-field velocity values have been investigated, to study the influence of Reynolds number and Mach number on the acoustic field. The reference conditions, presented in Table 1 have been taken from the experimental work of Brooks et al. [34].

4.2.1. Mean flow field

The mean flow calculations are made using a C-Type mesh with 125,000 cells, shown in Fig. 4. The grid clustering along the walls is such that the first interior cell is placed at y^+ of $O(1)$ for the all calculations, to accurately capture the turbulent kinetic energy peak. In Fig. 5a and b the iso-contours of mean velocity components U_x and U_y normalized with respect to the speed of sound, are plotted for test case 3. Similar results are obtained for the other cases. Fig. 6a shows the turbulent kinetic energy profiles along the wall normal at a station in correspondence of the trailing edge for the four cases. As expected, the peak of turbulent kinetic energy is more intense for higher Reynolds number values leading to stronger noise sources, being the amplitude of the Gaussian filter function of the turbulent kinetic energy (Eq. (20)). In Fig. 6b the profile of the specific dissipation ω_{Rans} at the same station is plotted in logarithmic scale. An increase in the boundary layer of the ω_{Rans} at higher values of the Reynolds number is evident, leading to smaller values of the turbulent length-scale (Eq. (21)). This behav-ior is shown in Fig. 7a where the boundary layer profile of the tur-bulent length-scale is presented. The length scale is evaluated with Eq. (21), where the length-scale limiter is switched off in order to compute the profile up to the wall.

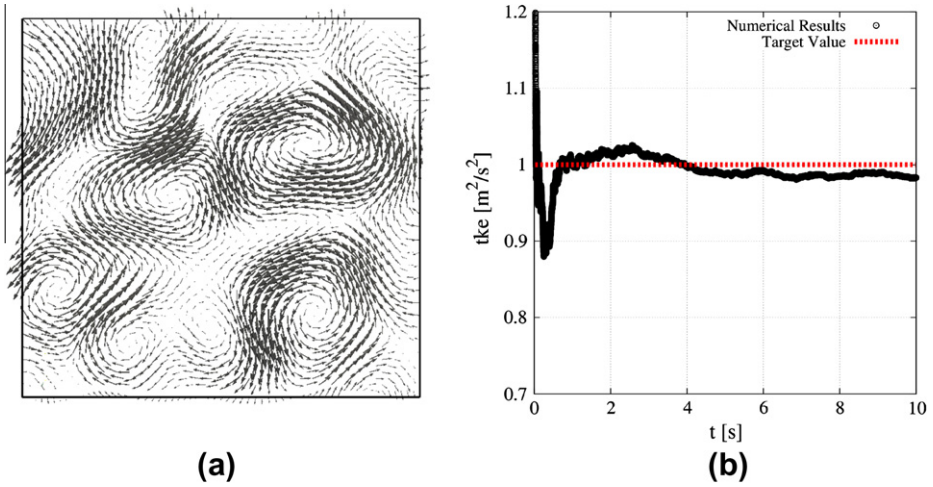

Fig. 1. Two-dimensional homogeneous and isotropic turbulence in a square: (a) turbulent velocity fluctuation vector plot, (b) turbulent kinetic energy time history.

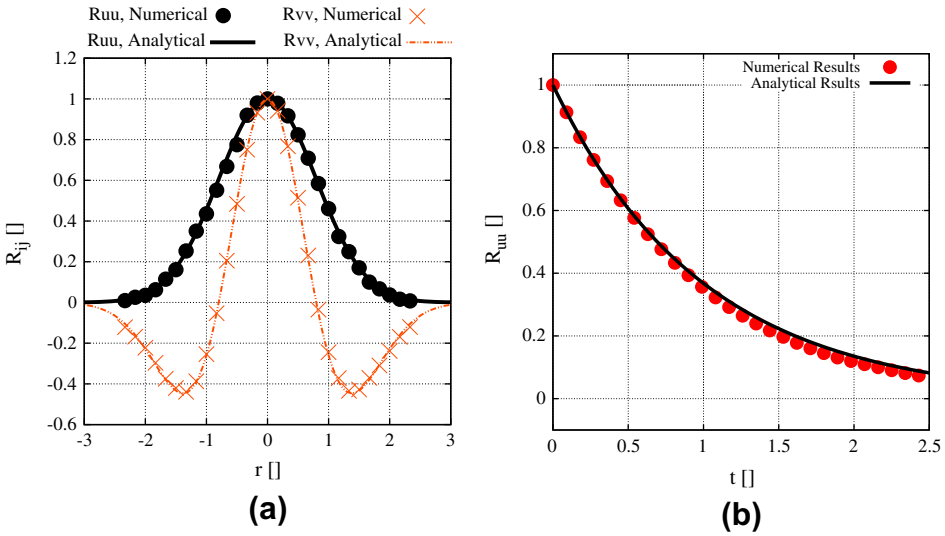

Fig. 2. Two-dimensional homogeneous and isotropic turbulence in a square: (a) normalized space correlations R_{uu} and R_{vv}, (b) normalized time autocorrelation function.

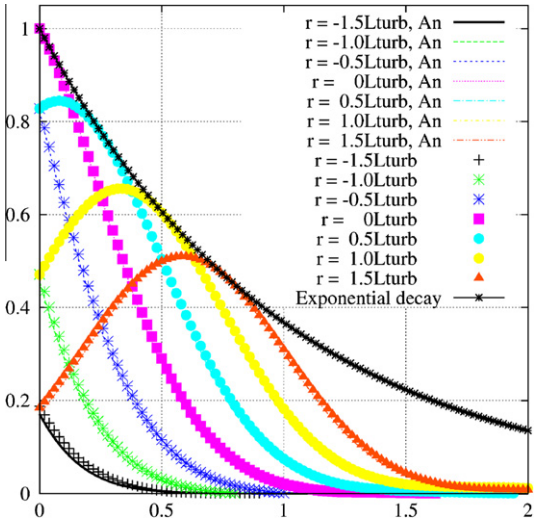

Fig. 3. Two-dimensional homogeneous and isotropic convected turbulence in a square: normalized cross-correlation function.

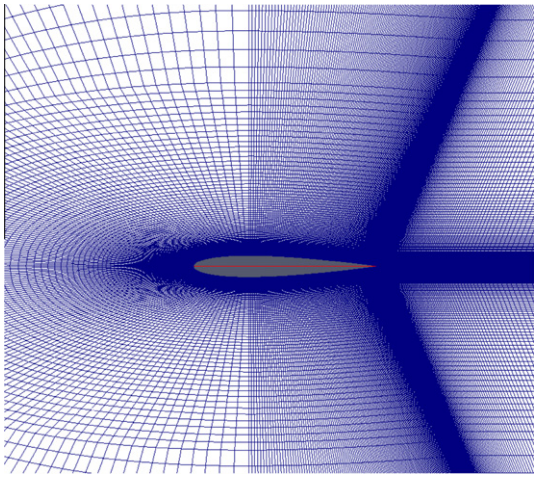

Fig. 4. CFD mesh, zoom in the airfoil region.

Table 1
Naca 0012, reference flow conditions.

Test case	c_0 (m/s)	U_0 (m/s)	Re (–)	M (–)
1	343	31.7	6.63×10^5	0.09
2	343	39.6	8.28×10^5	0.11
3	343	55.5	1.16×10^6	0.16
4	343	71.3	1.49×10^6	0.21

The boundary-layer thickness in the proximity of the trailing-edge in function of the Reynolds number has been compared with the experimental results of Brooks et al. [34]. The results are normalized with respect to the chord. Two sets of experimental data have been considered: the no tripped results (NT), and the heavily tripped results (HT). The former dataset is characterized by natural transition to turbulence, while in the latter transition is fixed at x/c = 0.2. In Fig. 7b, the boundary layer thickness δ is defined as the wall-distance where the total pressure becomes the 99.9% of the external value. The numerical results are in close agreement with the NT experimental data. In Fig. 8a and b, the displacement thickness δ^* and the momentum thickness θ are compared with the experimental results. The δ^* is in good agreement with the NT experimental data, while the θ values are slightly higher than the results of the same dataset. Brooks [34] reported that the tripping procedure produces a thicker boundary layer, and the present results confirm that the untripped boundary layer is thinner. The skin-friction coefficient, defined as

$$C_f = \frac{\tau_w}{\frac{1}{2}\rho_0 U_0^2}, \tag{31}$$

is plotted against the airfoil x-coordinate x/c in Fig. 9, for the four test conditions. The numerical results exhibit a fully turbulent behavior for the two higher Reynolds numbers, while for the lower Reynolds numbers the turbulent transition is achieved at about x/c = 0.07. The results of the two higher Re test cases are consistent with the HT experimental dataset, displaying a fully turbulent flow. But also in the two lower Reynolds cases transition is predicted well

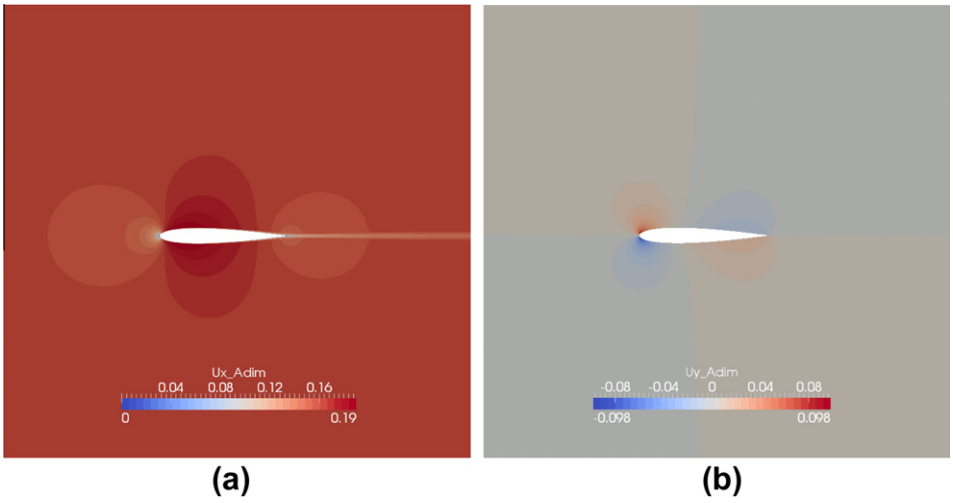

Fig. 5. Non-dimensional mean flow velocity iso-contours: (a) x-component , (b) y-component, test case 3, $Re = 6.63 \times 10^5$.

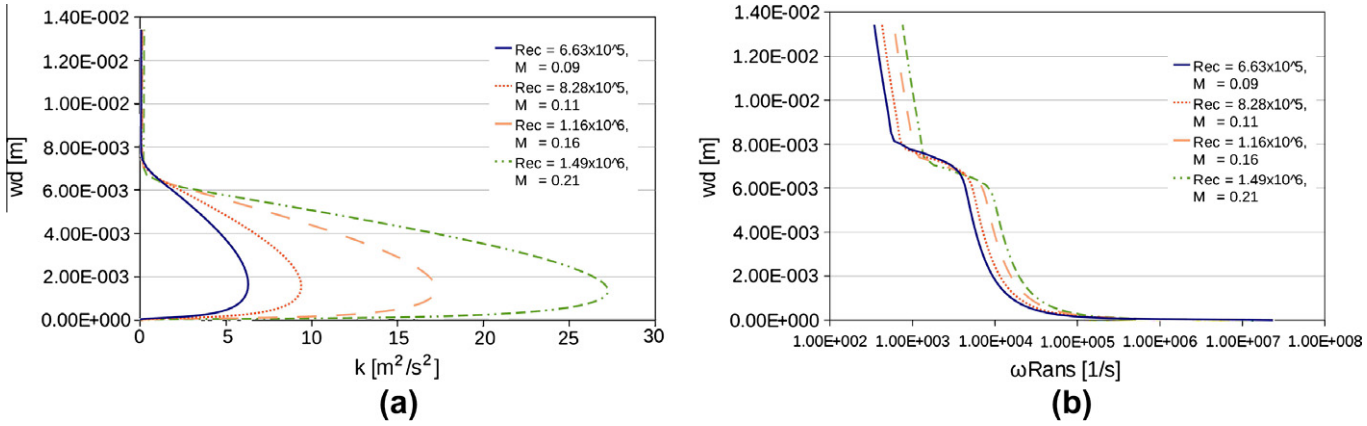

Fig. 6. Boundary-layer profiles: (a) turbulent kinetic energy (m^2/s^2), (b) specific dissipation (1/s).

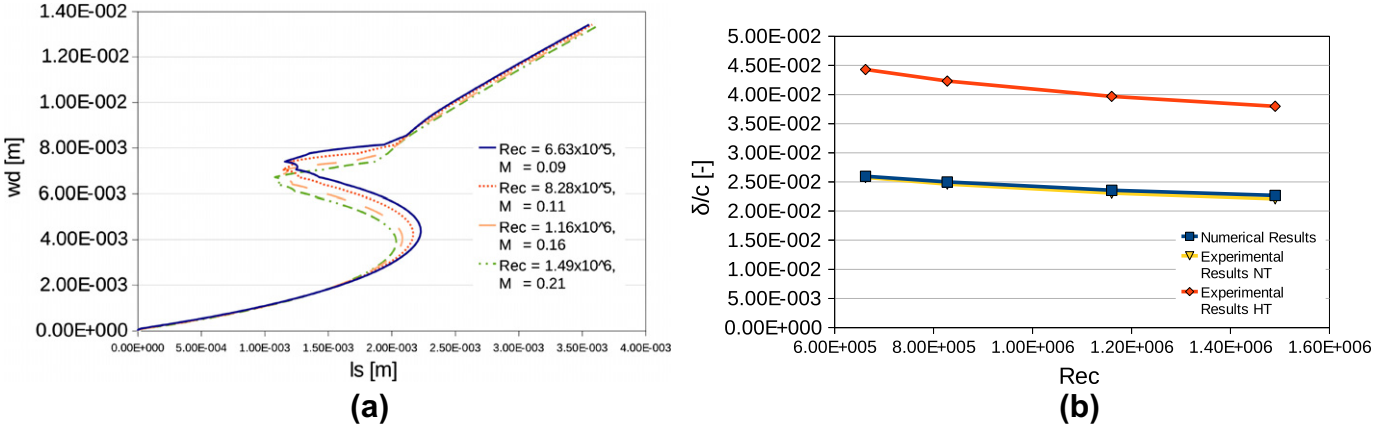

Fig. 7. (a) Boundary-layer profile of turbulent length-scale (m), (b) normalized boundary-layer thickness (–).

before the tripping location in the HT experiments. The fully turbulent flow as well as the early transition are due to the turbulence modeling. The k–ω SST model is lacking any information on transitional mechanisms. As a consequence, the numerical model predicts a flow field which is more consistent to the tripped experiments. The higher experimental boundary-layer thickness is mainly a collateral effect in the HT experiments for the presence of the tripping devices. Because the turbulent kinetic energy is strongly affecting the noise-source intensity [13], the acoustic results have been compared with the HT experimental results, under the assumption that the RANS solutions, even if they exhibit a thinner boundary layer, typical of an untripped flow field, have turbulent kinetic energy and specific dissipation values more consistent with the HT experiments.

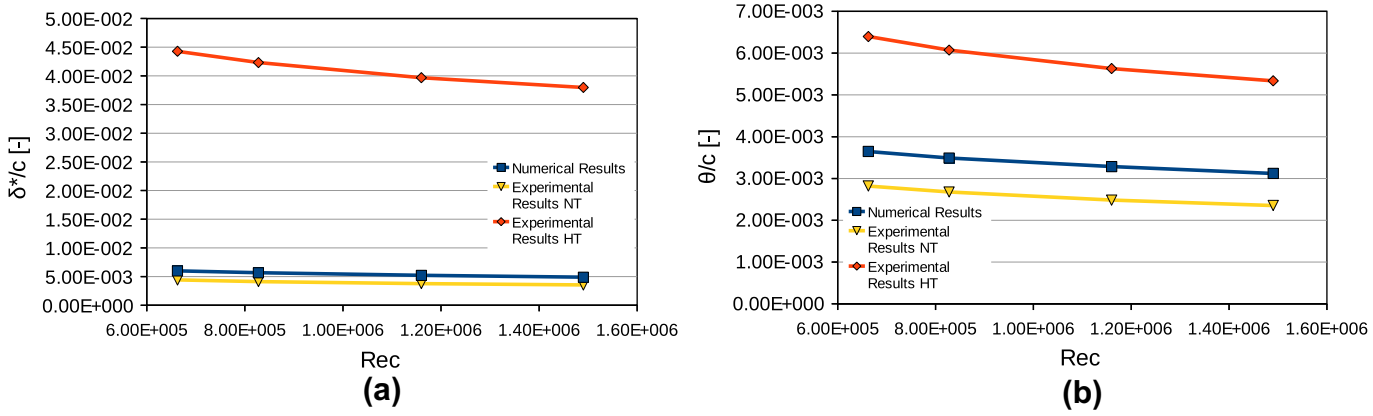

Fig. 8. (a) Normalized boundary-layer displacement thickness (–), (b) normalized boundary-layer momentum thickness (–).

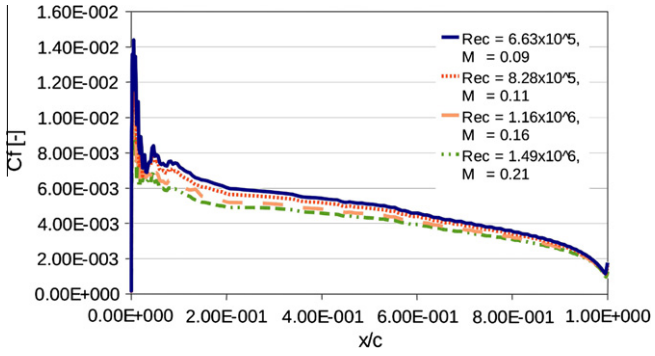

Fig. 9. Skin friction coefficient C_f (–).

4.2.2. Noise sources reconstruction

The noise source reconstruction is carried out on two symmetric patches placed on both sides of the airfoil, close to the trailing edge. The upper and lower boundaries of the patches are streamlines extracted as a postprocessing of the mean-flow solution. Each patch is discretized with a structured mesh of 400 × 40 rectangular elements. The turbulent length-scale limiter in Eq. (21) is set to 0.004 m, hence the smallest length-scale is resolved with at least 10 elements. A simulation time of 0.15 s has been adopted. The components S_2 and S_3 of the noise sources, defined in Eq. (28), are plotted in Fig. 10a and b at a given time for the test case 3 case. The S_3 component is one order of magnitude more intense than S_2 as expected. The source terms decay moving away from the wall, consistently with the non-homogeneous k field. Similar results are obtained for the other test cases.

4.2.3. Near-field acoustic results

The acoustic mesh, an hybrid triangular-quadrangular mesh with about *300,000* nodes, is plotted in Fig. 11. The acoustic domain extends from $-c$ to $2c$ in x-direction, and from $-c$ to c in y-direction and is surrounded by PML regions of thickness 0.1 m. Being the biggest cell size 5.2×10^{-3} m, the grid resolution is sufficient to compute frequencies up to 8500 Hz with at least 10 elements per wavelength for all tests. The grid is refined in the source region with a characteristic dimension of the smallest cell of 2×10^{-4} m, resolv-ing the smallest turbulence-induced wavelength with at least 18 elements. The source time history has been subdivided in segments 5.12×10^{-2} s long, with a time interval of 5×10^{-5} s and a maxi-mum overlap of 2.56×10^{-3} s. Each segment is transformed in the frequency domain using 1024 samples, with a base frequency of 19.531 Hz. In order to obtain a smoother spectrum, the transformed sources have been averaged over the five segments. A band-pass fil-ter has been applied to select frequencies between 200 Hz and 8500 Hz. Higher frequencies are not resolved by the mesh, and for the lower ones the time sampling is insufficient.

The near-field sound pressure level (SPL) at different Mach numbers are shown in Fig. 12a–d. The SPL values increase with the Mach number. The acoustic field displays a dipolar directivity, with the silence cone in front of the leading edge, due to the finite-ness of the airfoil. The main lobes are deflected in forward direc-tion, as result of the convective amplification. The normalized directivities for the four cases are shown in Fig. 13a at a radius r = 0.15 m. The numerical results are compared with the Ffowcs Williams and Hall analytical solution for a semi-infinite flat plate [35].

$$D_{n,FH}(\theta) = \sin\left(\frac{\theta}{2}\right). \tag{32}$$

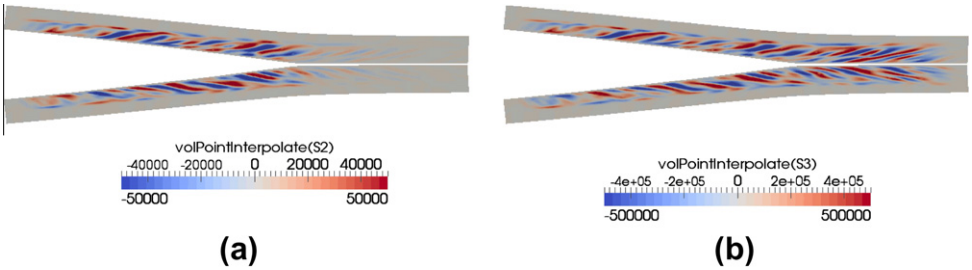

Fig. 10. Linearized Lamb vector snapshot: (a) S_2 (m/s^2), (b) S_3 (m/s^2).

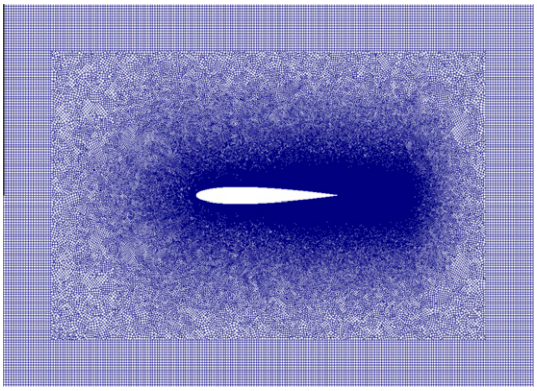

Fig. 11. Acoustic near-field mesh.

The computed directivities are normalized such that their value at 90° is equal to $D_{n,\,FH}(90°)$. The numerical predictions are in good agreement with the analytical results in the trailing edge region. Some discrepancies are present in the forward zone, mainly due to the airfoil thickness and leading edge diffraction effects, which are not taken into account by the analytical solution.

4.2.4. Far-field acoustic results

Normalized far-field directivities computed at r = 1.22 m, are presented in Fig. 13b. The typical leading edge diffraction effects and the Doppler shift are evident. The far-field directivities for four different wave numbers kc are presented in Fig. 14a–f. It can be noticed that while for the lowest frequency the pattern is almost dipolar, for the higher frequencies extra lobes appear in the directivity patterns. The numerical results at M = 0.16 are compared in Fig. 15a–d with the analytical prediction obtained with the trailing-edge noise model proposed by Roger and Moreau [29] for a finite-chord unloaded flat plate. The numerical results correctly predict the number and the angular location of the directivity lobes at each wave number. Differences with the analytical model are evident in the backward direction, mainly due to the zero thickness hypothesis of the analytical model.

The 1/3 octave power spectral densities (PSD) of the acoustic pressure in a probe point at r = 1.22 m and $\theta = 90°$ are shown in Fig. 16 and compared with the experimental results of Brooks et al. [34]. The parameters for the two-dimensional to three-dimensional correction are β = 1.68 and $U_c = 0.8U_\infty$, as suggested by experimental studies [36]. The agreement with the experimen-tal data in the frequency range between 1000 Hz to 6000 Hz is good. For high frequencies the decaying slope of the acoustic spec-trum is well captured and the difference between numerical re-sults and experiments is less than 3 dB. Largest discrepancies are present at the lower frequencies, due to a too short time sampling of the sources, leading to a poor averaging of the low frequencies.

In Fig. 17, the overall SPL (OASPL) values in function of the Mach number in the same probe location of the spectra are plotted. The numerical results are fitted by the following power law:

$$\mathrm{OASPL}_{Fit}(M) = 10\log[(M\ c_0)^{5.4}] - 9.743, \qquad (33)$$

with a maximum deviation of less than 0.8 dB. The resulting exponent of 5.4 is in good agreement with the theoretical value of 5, predicted by the Ffowcs Williams and Hall theory for the trailing-edge radiation of a semi-infinite flat plate. The prediction is in agreement with the value 5.6 given by Ewert et al. [13].

4.2.5. Computational requirements of the noise prediction procedures

All the calculations were performed on a Linux cluster, composed by 2 nodes, each node consisting in a two-way Quad-Core Xeon with 26 Gb of RAM. The CFD and the near-field propagation codes are parallelized with the MPI protocol, while the analytical noise routine,

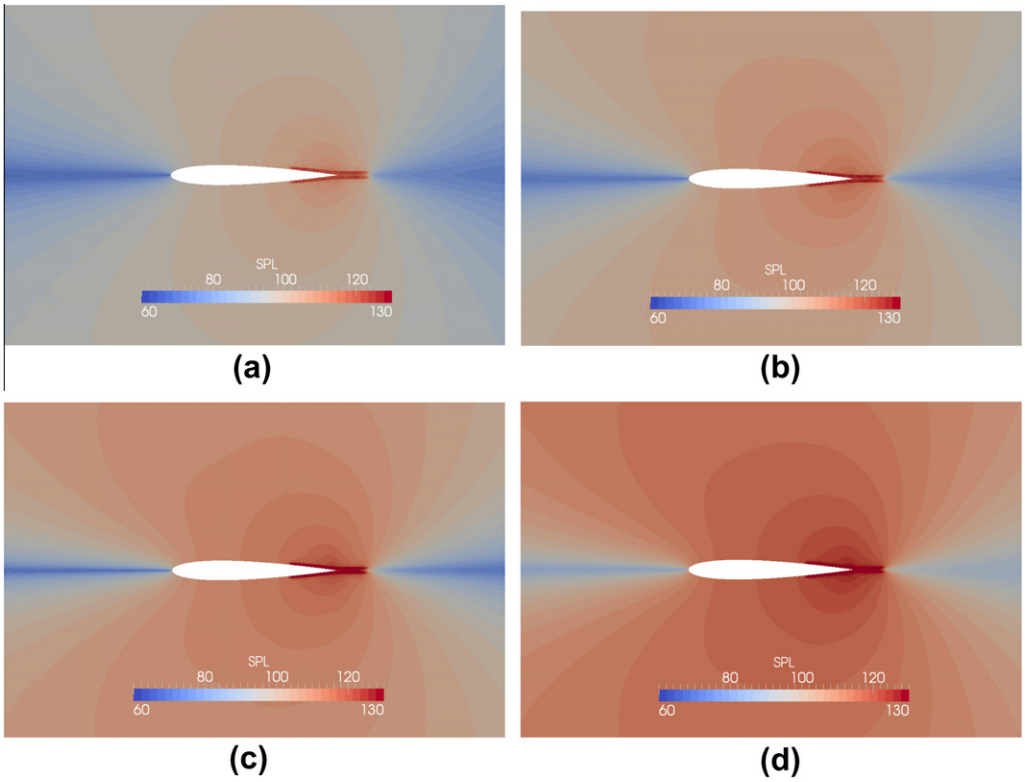

Fig. 12. Near-field SPL (dB): (a) M = 0.09, (b) M = 0.11, (c) test case 3, (d) M = 0.21.

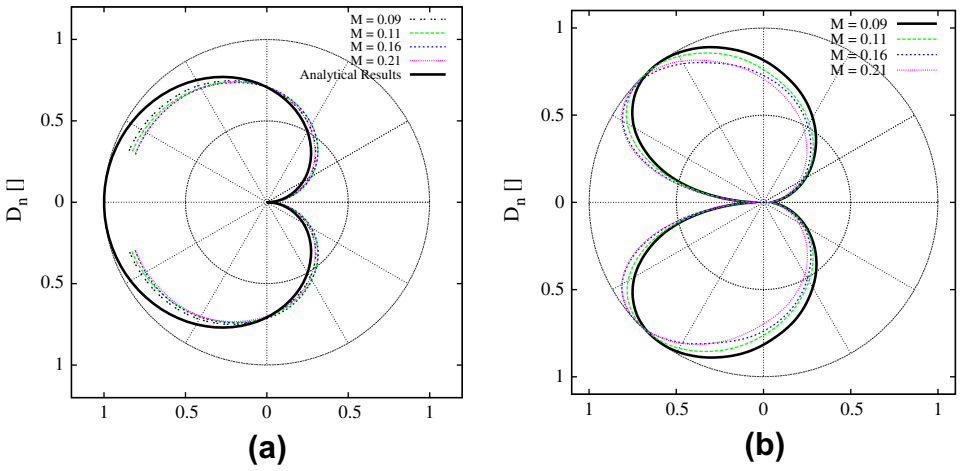

Fig. 13. (a) Near-field directivity (r = 0.15 m), (b) far-field directivity (r = 1.22 m).

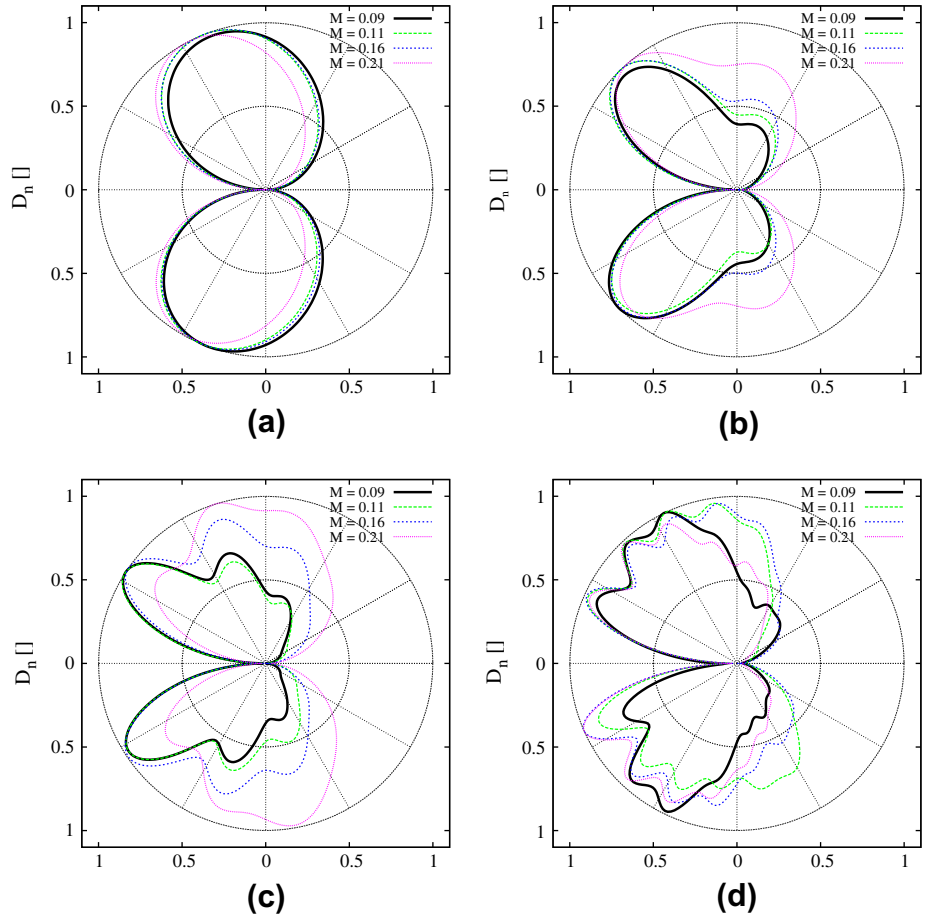

Fig. 14. Normalized far-field directivities (r = 1.22 m): (a) $kc \simeq 2$, (b) $kc \simeq 5$, (c) $kc \simeq 10$, (d) $kc \simeq 20$.

the noise-source reconstruction routines and the far-field propagation routine are scalar. Despite this, the analytical routine and the far-field propagation code run in few minutes for each computations, and as the noise-source fields are divided in independent regions, each patch can be computed simultaneously, reducing the total computational time for a single case. About four hours of computational time are necessary for computing a noise-source region with a grid of 16,000 cells and a simulation time of 0.15 s. The near-field noise computation with a grid of about 300,000 nodes takes about 12 h to evaluate 1024 frequencies. The APE equations are solved in the frequency domain, and the linear system is solved with a direct solver using the MUMPS (MUltifrontal Massively Parallel Solver) package [37]. One of the limiting factor for these cal-culations is the RAM requirements: for the above calculations 12 Gb

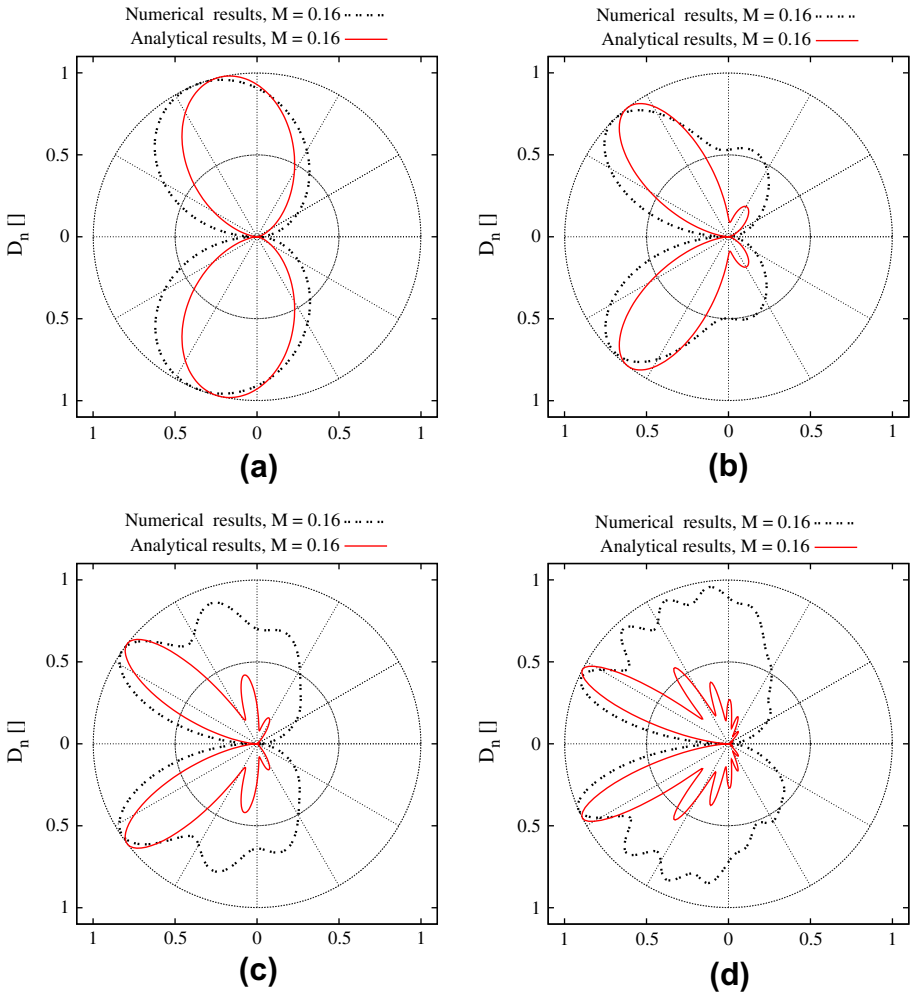

Fig. 15. Normalized far-field directivities ($r = 1.22$ m, $M = 0.16$), numerical results compared with the analytical predictions (Roger and Moreau model): (a) $kc \simeq 2$, (b) $kc \simeq 5$, (c) $kc \simeq 10$, (d) $kc \simeq 20$.

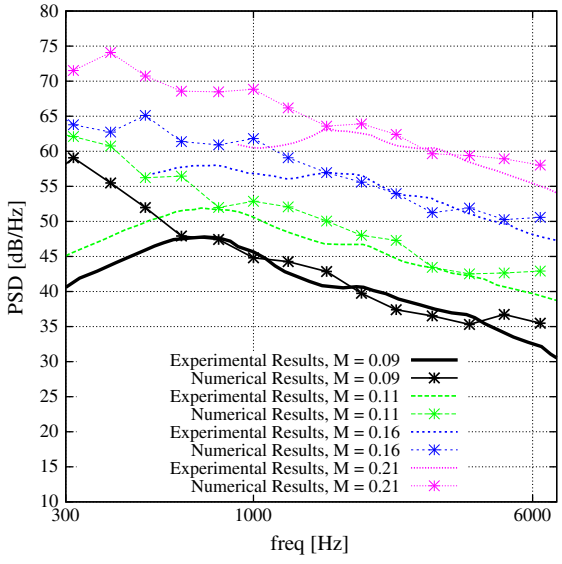

Fig. 16. Far-field acoustic pressure PSD ($r = 1.22$ m, $\theta = 90°$).

of RAM are required. A complete calculation, consisting in the CFD calculation, the reconstruction of the noise sources, and a near and far-field calculations, takes about 18 h on the whole.

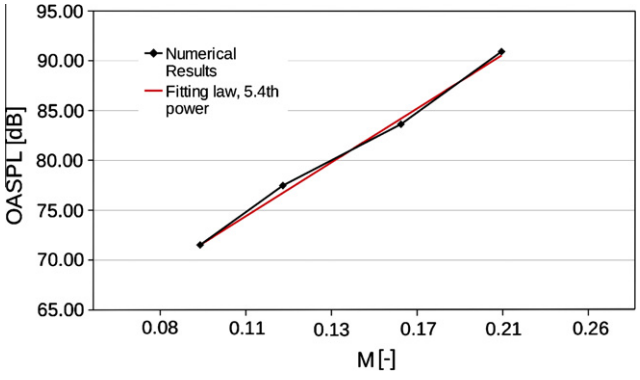

Fig. 17. OASPL (dB) ($r = 1.22$ m, $\theta = 90°$), Mach number scaling law.

5. Conclusions

The method termed ESDF, a RANS-based stochastic source modeling for the numerical prediction of broadband trailing-edge noise, has been presented. It generates a solenoidal fluctuating turbulent velocity field, reproducing the turbulence statistics provided by the RANS simulations. The ESDF method has been validated with a homogeneous and isotropic turbulence in a

two-dimensional square. The numerical results were in good agreement with the analytical predictions.

Then the ESDF method has been applied to a low Mach number trailing-edge noise problem. The stochastic source model has been coupled with a frequency-domain Galerkin Finite Element solver of the Acoustic Perturbation Equations for the near-field region. Far-field directivities and spectra have been evaluated with the Ffowcs Williams and Hawkings integral formulation. The predicted noise levels for a NACA 0012 airfoil, at zero incidence and at different Mach and Reynolds numbers, have been compared with experimental and analytical results. A good agreement in the frequency range of 1000–6000 Hz has been obtained. Though improvements are needed in order to extend the generation procedure for dealing with three-dimensional computations and anisotropic turbulence statistics, the proposed method has been proved to be a fast and reliable tool for aeroacoustic design and optimization.

References

[1] Howe MS. A review of the theory of trailing edge noise. J Sound Vib 1978:437–66.

[2] Casalino D, Moreau S, Roger M. One, no one and one hundred thousand methods for low-speed fan noise prediction. Aeroacoustics 2010;9(3):307–27.

[3] Glegg S, Morin B, Atassi O, Reba R. Using Reynolds-averaged Navier–Stokes calculations to predict trailing edge noise. AIAA J 2010;48(7):12901301.

[4] Kraichnan R. Diffusion by a random velocity field. Phys Fluids 1994;13:22–31.

[5] Béchara W, Bailly C, Lafon P, Candel SM. Stochastic approach to noise modelling for free turbulent flows. AIAA J 1994;32(3).

[6] Bailly C, Lafon P, Candel SM. Subsonic and supersonic jet noise predictions from statistical source models. AIAA J 1997;35(11).

[7] Billson M. Computational techniques for turbulence generated noise. PhD thesis. Chalmers University of Technology; 2004.

[8] Ewert R, Bauer M. Towards the prediction of broadband trailing edge noise via stochastic surface sources. In: AIAA Paper 2004-2861; 2004.

[9] Casalino D, Barbarino M. A stochastic method for airfoil self-noise computations in frequency-domain. In: AIAA Paper 2010-3884; 2010.

[10] Careta A, Saugés F, Sancho JM. Stochastic generation of homogeneous isotropic turbulence with well-defined spectra. Phys Rev E 1993;48(3):2279–87.

[11] Klein M, Sadiki A, Janicka J. A digital filter based generation of inflow data for spatially developing direct numerical or large eddy simulations. J Computat Phys 2003;186:652–65.

[12] Ewert R. Broadband slat noise prediction based on CAA and stochastic sound sources from a fast random particle-mesh (RPM) method. Comput Fluids 2008:369–87.

[13] Ewert R, Appel C, Dierke J, Herr M. RANS/CAA based prediction of naca 0012 broadband trailing edge noise and experimental validation. In: 15th AIAA/CEAS aeroacoustics conference. Miami, Florida, AIAA Paper 2009-3269; May 2009.

[14] Mühlbauer B, Ewert R, Koronow O, Noll B, Delfs JW, Aigner M. Simulation of combustion noise using CAA with stochastic sound sources from RANS. In: 14th AIAA/CEAS aeroacoustics conference. Vancouver, Canada, AIAA Paper 2008-2944; May 2008.

[15] Siefert M, Ewert R, Heintze O, Unruh O. A synthetic wall pressure model for the efficient simulation of boundary layer induced cabin noise. In: 16th AIAA/CEAS aeroacoustics conference. Stockholm, Sweden, AIAA Paper 2010-3760; 2010.

[16] Dieste M, Gabard G. Random-vortex-particle method for broadband fan interaction noise. In: 16th AIAA/CEAS aeroacoustics conference. Stockholm, Sweden, AIAA Paper 2010-3885; 2010.

[17] Mesbah Majid. Flow Noise prediction using the stochastic noise generation and radiation approach. PhD thesis. Katholieke Universiteit Leuven; 2006.

[18] Billson M, Eriksson LE, Davidson L. Jet noise modeling using synthetic anisotropic turbulence. In: AIAA Paper 2004-3028; 2004.

[19] Bailly C, Juvé D. A stochastic approach to compute subsonic noise using linearized euler equations. In: AIAA Paper 2004-2857; 2004.

[20] OpenFOAM®; 2009. <http://www.opencfd.co.uk/openfoam> [last update 28.07.09].

[21] Menter FR. Two-equation eddy-viscosity turbulence models for engineering applications. AIAA J 1994;32(8).

[22] Jasak H, Weller HG, Gosman AD. High resolution NVD differencing scheme for arbitrary unstructured meshes. Int J Numer Methods Fluids 1999;31:431–49.

[23] Geuzaine C, Remacle J-F. A three-dimensional finite element mesh generator with built-in pre- and post-processing facilities. Int J Numer Methods Eng 2009;79(11):1309–31.

[24] Carton de Wiart C, Georges L, Geuzaine P, Detandt Y, Caro S. Analysis of the noise source interpolation within a hybrid caa method: application to the case of the Hlemholtz resonator. In: AIAA Paper 2009-3115; 2009.

[25] Bauer M, Zeibig A, Koltzsch P. Application of the SNGR-model to compute trailing edge noise. Technical Report. Dresden University of Technology; 2006.

[26] Seo JH, Moon YJ. Aerodynamic noise prediction for long-span bodies. J Sound Vib 2007(306):564–79.

[27] Corcos GM. The structure of the turbulent pressure field in boundary-layer flows. J Fluid Mech 1964;18:353–78.

[28] Rozenberg Y. Modlisation analytique du bruit arodynamique large bande des machines tournantes: utilisation de calculs moyenns de mcanique des fluides. PhD thesis. LMFA, Ecole Centrale de Lyon; 2007.

[29] Roger M, Moreau S. Back-scattering correction and further extensions of Amiet's trailing-edge noise model. Part 1: Theory. J Sound Vib 2005(286):477–506.

[30] Gruber M, Joseph PF. Private communication; 2010.

[31] Iob A, Arina R, Schipani C. A frequency-domain linearized Euler model for turbomachinery noise radiation through engine exhaust. AIAA J 2010;48(4):848–58.

[32] Hu Fang Q. A stable, perfectly matched layer for linearized euler equations in unsplit physical variables. J Computat Phys 2001;173:455–80.

[33] Arina R, Malvano R, Piccato A, Spazzini PG. Numerical and experimental analysis of sound generated by an orifice. In: AIAA Paper 2007-3404; 2007.

[34] Brooks T, Pope D, Marcolini M. Airfoil self-noise and prediction. Technical Report. Technical Report. NASA, Reference Publication 1218; 1989.

[35] Ffowcs Williams JE, Hall LH. Aerodynamic sound generation by turbulent flow in the vicinity of a scattering half plane. J Fluid Mech 1970;40(4):657–70.

[36] Amiet RK. Noise due to turbulent flow past a trailing edge. J Sound Vib 1976;3(47):387–93.

[37] Guermouche A, Amestoyand PR, et al. Hybrid scheduling for the parallel solution of linear system. Parallel Comput 2006;32(2):136–56.